RSC Advances

PAPER

View Article Online
View Journal | View Issue

Cite this: *RSC Adv.*, 2022, **12**, 10675

Tuning composition of $CuCo_2S_4$–$NiCo_2S_4$ solid solutions *via* solvent-less pyrolysis of molecular precursors for efficient supercapacitance and water splitting†

Ginena Bildard Shombe,[ab] Malik Dilshad Khan, *[ac] Jonghyun Choi,[d] Ram K. Gupta,[d] Marcin Opallo[c] and Neerish Revaprasadu *[a]

Mixed metal sulfides are increasingly being investigated because of their prospective applications for electrochemical energy storage and conversion. Their high electronic conductivity and high density of redox sites result in significant improvement of their electrochemical properties. Herein, the composition-dependent supercapacitive and water splitting performance of a series of $Ni_{(1-x)}Cu_xCo_2S_4$ ($0.2 \leq x \leq 0.8$) solid solutions prepared *via* solvent-less pyrolysis of a mixture of respective metal ethyl xanthate precursors is reported. The use of xanthate precursors resulted in the formation of surface clean nanomaterials at low-temperature. Their structural, compositional, and morphological features were examined by p-XRD, SEM, and EDX analyses. Both supercapacitive and electrocatalytic (HER, OER) properties of the synthesized materials significantly vary with composition (Ni/Cu molar content). However, the optimal composition depends on the application. The highest specific capacitance of 770 F g^{-1} at a current density of 1 A g^{-1} was achieved for $Ni_{0.6}Cu_{0.4}Co_2S_4$ (NCCS-2). This electrode exhibits capacitance retention (C_R) of 67% at 30 A g^{-1}, which is higher than that observed for pristine $NiCo_2S_4$ (838 F g^{-1} at 1 A g^{-1}, 47% C_R at 30 A g^{-1}). On the contrary, $Ni_{0.4}Cu_{0.6}Co_2S_4$ (NCCS-3) exhibits the lowest overpotential of 124 mV to deliver a current density of 10 mA cm^{-2}. Finally, the best OER activity with an overpotential of 268 mV at 10 mA cm^{-2} was displayed by $Ni_{0.8}Cu_{0.2}Co_2S_4$ (NCCS-1). The prepared electrodes exhibit high stability, as well as durability.

Received 7th February 2022
Accepted 28th March 2022

DOI: 10.1039/d2ra00815g

rsc.li/rsc-advances

1 Introduction

The formation of solid solutions provides an excellent opportunity for tuning the physicochemical properties of materials.[1] Unlike size and shape manipulation,[2] material properties are optimized by changing composition.[3,4] In some instances, this is achieved by incorporating an ion or atom in the interstices of the host lattice.[5] When the sizes of the components involved are comparable, mutual substitution of the species occurs, and the substituent(s) resides in equivalent crystallographic positions.[3,5] Specifically, the formation of solid solutions is governed by a set of Hume-Rothery rules.[6] Depending on the size of the solute component, an increase or decrease of the host lattice parameters occurs, which in turn causes an expansion or contraction of the cell.[3,4,7] This type of property tailoring has facilitated the development of various optoelectronic devices and the generation of clean energy.[1] It also provides an opportunity for the tuning of electrocatalytic properties and energy storage capacity of electrode materials.[8,9] However, this method of electrode material optimization remains relatively unexplored for metal chalcogenides.

Transition metal sulfides (TMS) are amongst the most explored materials for energy-related applications.[10] This is a part of the ongoing effort to search for earth-abundant, inexpensive, and highly effective materials for energy storage and/or conversion technologies.[11,12] TMS exhibit high electronic conductivity, capacitance, and redox reversibility. They also possess good mechanical and thermal stability relative to various metal oxides, and non-transition metal-based materials.[10] In comparison to binary metal sulfides, the multiple valences of cations in mixed metal sulfides is their specific advantage as they synergistically affect the electrochemical properties of the materials, and increase the overall efficiency.[13] For instance, the electrochemical investigation of $Sb_2(S_{1-x}Se_x)_3$

[a]*Department of Chemistry, University of Zululand, Private Bag X1001, KwaDlangezwa 3880, South Africa. E-mail: RevaprasaduN@unizulu.ac.za*

[b]*Chemistry Department, University of Dar-es-Salaam, P. O. Box 35091, Dar es Salaam, Tanzania*

[c]*Institute of Physical Chemistry, Polish Academy of Sciences, Kasprzaka 44/52, 01-224 Warsaw, Poland. E-mail: malikdilshad@ichf.edu.pl*

[d]*Department of Chemistry, Kansas Polymer Research Center, Pittsburg State University, Pittsburg, KS 66762, USA*

† Electronic supplementary information (ESI) available. See DOI: 10.1039/d2ra00815g

($0 \leq x \leq 1$) over the entire range indicated that the alloyed compositions showed better electrochemical performance than the binary antimony chalcogenides.[8]

Ternary metal sulfides $NiCo_2S_4$ and $CuCo_2S_4$ have gained recent attention. They both occur as regular thiospinels where the divalent cations fill the tetrahedral positions, and the trivalent cations fill the octahedral positions.[14] $NiCo_2S_4$ has demonstrated excellent electrochemical performance in supercapacitors,[15] batteries,[16] dye-sensitized solar cells,[17] oxygen reduction/evolution reactions,[18] and hydrogen generation reactions.[19] This remarkable performance is thought to be a result of its metallic nature.[20] On the other hand, $CuCo_2S_4$ has mainly been investigated for energy storage applications,[21–23] and a few studies on energy generation applications are found in the literature.[24,25]

To improve the electrochemical properties of the two systems, various strategies such as doping and formation of hybrid materials have been employed. For instance, Zhang *et al.* employed a multi-step hydrothermal calcination approach to prepare Cu-doped $NiCo_2S_4$ flower-like nanosheet arrays which displayed a high specific capacitance of 2044 F g^{-1} as compared to the undoped $NiCo_2S_4$ nanostructures which showcased a specific capacitance of 1268 F g^{-1}. It was further shown that coupling the Cu-doped $NiCo_2S_4$ nanosheet arrays with flake graphite significantly enhances the capacity to over twice that of pristine $NiCo_2S_4$.[26] Hybrids of $NiCo_2S_4$ or $CuCo_2S_4$ and graphene,[21] carbon nanotubes,[27] polymers[28] or other ternary systems[29,30] have also been investigated as potential candidates for energy storage and/or generation. However, it is surprising to note very few attempts on the generation of solid solutions of the two systems.[31] $NiCo_2S_4$ and $CuCo_2S_4$ are isostructural, and the respective divalent cations have comparable ionic radii (Ni^{2+}, 0.69 Å; Cu^{2+}, 0.73 Å),[32] and similar electronegativity (1.91 for Ni, and 1.90 for Cu). Therefore, they comply with the Hume-Rothery rules, and a substitutional solid solution is viable over the entire composition range. Furthermore, the report by Wagner and Cook on the solid solutions of carrollite and related minerals confirms the natural existence of the Cu–Co–Ni–S solid solutions.[33]

Generally, the preparation of nanostructured crystalline solid solutions is rather difficult and challenging. Crystal defects and/or phase separation may occur depending on the synthetic strategy and growth parameters employed. To ensure the formation of a homogeneous solid solution, a well-designed synthetic protocol and precise control of reaction parameters are required.[1] A recently proposed approach, based on the solvent-less pyrolysis of respective single molecular precursors is one of the possibilities.[34] This approach is simple, cost-effective, scalable, and has proven efficient for preparing numerous nanostructured materials of good quality.[34] More importantly, this method offers the possibility of preparing nanomaterials with surfaces free of surfactants.[35,36] This provides the likelihood of synthesizing materials with abundant exposed active sites and enhanced (electro)catalytic performance.[37] Nevertheless, this approach has not been largely explored for the preparation of nanostructured solid solutions.[4,38] Herein, we report the synthesis of $Ni_{(1-x)}Cu_xCo_2S_4$ ($x =$ 0.2, 0.4, 0.6, and 0.8) solid solutions *via* the solvent-less thermolysis of the respective metal ethyl xanthate precursors at 250 °C. The choice of metal xanthate precursors of the short alkyl chain is based on the possibility of synthesizing nanomaterials free of capping ligands and improved catalytic activity.[35] We will demonstrate that supercapacitive properties and efficiency of water splitting depend on the composition of mixed sulfides studied.

2 Experimental

2.1 Chemicals

Potassium ethyl xanthogenate (96%, Sigma-Aldrich); cupric chloride dihydrate (97%, Saarchem); cobalt(II) acetate tetrahydrate (98%, Saarchem), and nickel(II) acetate tetrahydrate, chloroform (min 99%), and acetone purchased from Merck chemicals. All chemicals were used as received.

2.2 Synthesis of precursors

2.2.1. Synthesis of metal (Co, Cu, Ni) xanthate complexes. The synthesis of metal xanthate complexes is well known and was performed by following previously reported methods with slight modifications.[39] Briefly, to obtain nickel ethyl xanthate (**1**), nickel acetate tetrahydrate (1.2443 g, 5.0 mmol) was dissolved in distilled water (25.0 mL), followed by its drop-wise addition to the solution of potassium ethyl xanthogenate (1.603 g, 10.0 mmol). The reaction mixture was stirred for 1 hour, after which the formed precipitate was washed with distilled water, dried under vacuum, and recrystallized from chloroform. Elemental analysis for $C_6H_{10}O_2S_4Ni$: calc. C, 23.91%; H, 3.35%; S, 42.51%. Found: C, 23.81%; H, 3.2%; S, 42.17%.

The synthetic procedure used to prepare complex (**1**) was followed to prepare copper ethyl xanthate (**2**) and cobalt ethyl xanthate (**3**) complexes as well. Elemental analysis for $C_6H_{10}O_2S_4Cu$ (complex (**2**)): calc. C, 23.57%; H, 3.30%; S, 41.86%. Found: C, 23.1%; H, 3.14%; S, 41.16%. Elemental analysis for $C_6H_{10}O_2S_4Co$ (complex (**3**)): calc. C, 23.93%; H, 3.35%; S, 42.50%. Found: C, 22.03%; H, 3.33%; S, 41.09%.

2.3 The solvent-less synthesis of $Ni_{(1-x)}Cu_xCo_2S_4$ ($x = 0$, 0.2, 0.4, 0.6, 0.8, and 1)

Stoichiometric quantities of the required complexes were mixed to obtain a homogenized mixture. A ceramic boat containing a mixture of the complexes was placed at the center of a quartz tube and inserted in the furnace. The sample was then heated at 250 °C for one hour under N_2 flow. The product formed after the specified time was cooled naturally to room temperature and collected for further analyses.

2.4 Characterization

Elemental analysis was performed on a PerkinElmer automated model 2400 series II CHNS/O analyzer. TGA of the complexes was carried out at a 10 °C min^{-1} heating rate using a PerkinElmer Pyris 6 TGA up to 600 °C in a closed perforated aluminum pan under N_2 gas flow. Powder diffraction patterns

of the ternary systems and the solid solutions were recorded in the high angle 2θ range of 10–80° using a Bruker AXS D8 diffractometer equipped with a nickel-filtered Cu Kα radiation ($\lambda = 1.5418$ Å) at 40 kV, 40 mA at room temperature. The scan speed was 0.5 s per step at an increment of 0.01314. TEM analysis of the samples was carried out using a JEOL 1400 TEM, whereas HRTEM analysis was carried out on a JEOL 2100 HRTEM. Samples were prepared by placing a drop of the particles' dilute solution on Formvar-coated grids (150 mesh) for TEM, and holey carbon grids for HRTEM. The samples were allowed to dry completely at room temperature, viewed at accelerating voltages of 120 kV for TEM, and 200 kV for HRTEM. Images were captured digitally using a Megaview III camera; stored and measured using soft imaging systems iTEM software (TEM) and Gatan camera with Gatan software (HRTEM). SEM and EDX analyses were performed on ZEISS-Auriga Cobra SEM and ZEISS ultra plus field emission gun scanning electron microscope respectively.

2.5 Electrochemical studies

Electrochemical characterization of the synthesized materials was performed using Gamry Potentiostat using a three-electrode system. A paste consisting of the synthesized sample (80 wt%), acetylene black (10 wt%), and polyvinylidene difluoride (PVDF, 10 wt%) was prepared using *N*-methyl pyrrolidinone (NMP) as a solvent.[40] This paste was then deposited to pre-cleaned and weighted nickel foam. The paste deposited on nickel foam was then dried under vacuum at 60 °C for 10 hours and used as a working electrode. A platinum wire and saturated calomel electrode (SCE) or Hg/HgO were used as counter and reference electrodes, respectively. All the experiments for energy storage and electrocatalysis were performed using 3 M and 1 M KOH electrolyte, respectively. Hg/HgO was used for supercapacitor testing while saturated calomel electrode was used for water splitting applications. Charge storage capacity was measured using cyclic voltammetry (CV) and galvanostatic charge–discharge (GCD) at various scan rates and current densities, respectively. Electrocatalytic properties of the synthesized electrodes were studied using linear sweep voltammetry (LSV), cyclic voltammetry, and chronoamperometry (CA). LSV was performed at a scan rate of 2 mV s^{-1} for both OER and HER measurements. Electrochemical impedance spectroscopy (EIS) was performed during all the tests in the frequency range of 0.05 Hz to 10 kHz with an applied AC amplitude of 10 mV.

3 Results and discussion

3.1 Characterization of the precursors and $Ni_{(1-x)}Cu_xCo_2S_4$ ($0 \leq x \leq 1$)

Complexes (**1**), (**2**), and (**3**) were synthesized using a known synthetic procedure,[39] and characterized by elemental analysis (CHNS) and IR spectroscopy. Thermogravimetric analysis was also carried out to investigate the thermal decomposition behavior of the complexes (Fig. S1, ESI†). A single-step decomposition of precursor to respective metal sulfides is observed for all complexes. Complex (**1**) decomposes in the temperature range of 132–228 °C with a weight loss of 72% and a residual weight of 28%, which matches closely with NiS (29%). A relatively lower onset temperature of *ca.* 77 °C was observed for complex (**2**), and complete decomposition of the precursor occurs at 210 °C. 30% of the initial weight, which compares well with the theoretical value of CuS (31%), was left as the final residue. On the other hand, complex (**3**) shows decomposition at 203 °C with an onset temperature of 96 °C. A 27% residual weight which corresponds to the theoretical weight calculated for CoS (29%), was observed. All complexes decompose at fairly low temperatures, which indicates the possibility of the low-temperature synthesis of the intended solid solutions. Clearly, low melting point and moderate decomposition temperature make xanthates favorable precursors for the melt synthesis of metal sulfides. Furthermore, the generated by-products (carbonyl sulfide and alkene) are highly volatile, and hence pure metal sulfides are obtained.[41] The pyrolysis temperature for the synthesis of the solid solutions was therefore chosen to be 250 °C.

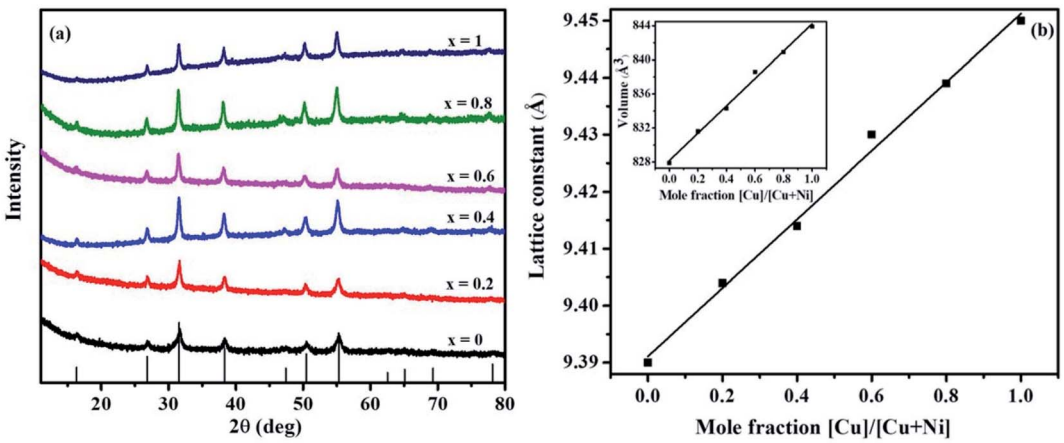

Fig. 1 (a) p-XRD patterns of $Ni_{(1-x)}Cu_xCo_2S_4$ ($x = 0$, 0.2, 0.4, 0.6, 0.8, and 1). (b) Lattice parameters of $Ni_{(1-x)}Cu_xCo_2S_4$ ($x = 0$, 0.2, 0.4, 0.6, 0.8 and 1) and the corresponding cell volumes (inset) as a function of copper mole fraction in precursor feed.

Table 1 Lattice parameters, cell volumes, average crystallite sizes, and theoretical and experimental mole compositions of $Ni_{(1-x)}Cu_xCo_2S_4$ (x = 0, 0.2, 0.4, 0.6, 0.8 and 1)

Copper mole fraction, x	Cell constant a (Å)	Cell volume (Å^3)	Particle size from Scherrer equation (nm)	Theoretical composition	Experimental composition
0	9.390	827.9	9.6	$NiCo_2S_4$	$Ni_{1.2}Co_2S_{3.8}$
0.2	9.404	831.6	12.8	$Ni_{0.8}Cu_{0.2}Co_2S_4$	$Ni_{0.84}Cu_{0.21}Co_2S_{3.9}$
0.4	9.414	834.3	14.2	$Ni_{0.6}Cu_{0.4}Co_2S_4$	$Ni_{0.63}Cu_{0.45}Co_{2.1}S_{3.8}$
0.6	9.430	838.6	19.2	$Ni_{0.4}Cu_{0.6}Co_2S_4$	$Ni_{0.41}Cu_{0.61}Co_{2.1}S_{3.9}$
0.8	9.439	840.9	19.1	$Ni_{0.2}Cu_{0.8}Co_2S_4$	$Ni_{0.25}Cu_{0.86}Co_{1.9}S_{3.9}$
1	9.450	843.9	16.4	$CuCo_2S_4$	$Cu_{0.8}Co_{2.1}S_{4.0}$

Since $NiCo_2S_4$ and $CuCo_2S_4$ comply with the Hume-Rothery rules, the formation of Ni–Cu–Co–S primary solid solutions is therefore feasible. Therefore, solid solutions were prepared by heating stoichiometric mixtures of complexes (**1**), (**2**), and (**3**) at 250 °C under nitrogen for 1 hour. For comparison, pure $NiCo_2S_4$ and $CuCo_2S_4$ were also prepared by heating a mixture of the two respective metal ethyl xanthate complexes under similar conditions. The formed materials were characterized by p-XRD, SEM, TEM, and EDX.

The p-XRD patterns of $Ni_{(1-x)}Cu_xCo_2S_4$ ($0 \leq x \leq 1$) are presented in Fig. 1a. The diffraction peaks of the ternary systems prepared at $x = 0$ and $x = 1$ are consistent with the pure cubic phases of $NiCo_2S_4$ (ICDD #: 00-020-0782) and $CuCo_2S_4$ (ICDD #: 00-042-1450) respectively, whereas the diffraction peaks of the solid solutions (x = 0.2, 0.4, 0.6 and 0.8) lie between those of $NiCo_2S_4$ and $CuCo_2S_4$. The Cu^{2+} ions introduced into $NiCo_2S_4$ are expected to occupy some of the tetrahedral sites of the cubic unit cell. Considering that Cu^{2+} is slightly larger than Ni^{2+},[32] this is expected to produce a slight shift in the peak positions. As seen from the extended part of the diffraction patterns, the peak positions show a gradual shift towards lower angles with increasing copper concentration (Fig. S2, ESI†). This suggests that Cu^{2+} has been incorporated into the $NiCo_2S_4$ lattice system. The lattice parameters of all the synthesized materials were calculated from the p-XRD data using the relation $1/d^2 = (h^2 + k^2 + l^2)/a^2$ (Table 1). The lattice parameters of $NiCo_2S_4$ ($a = b = c$)

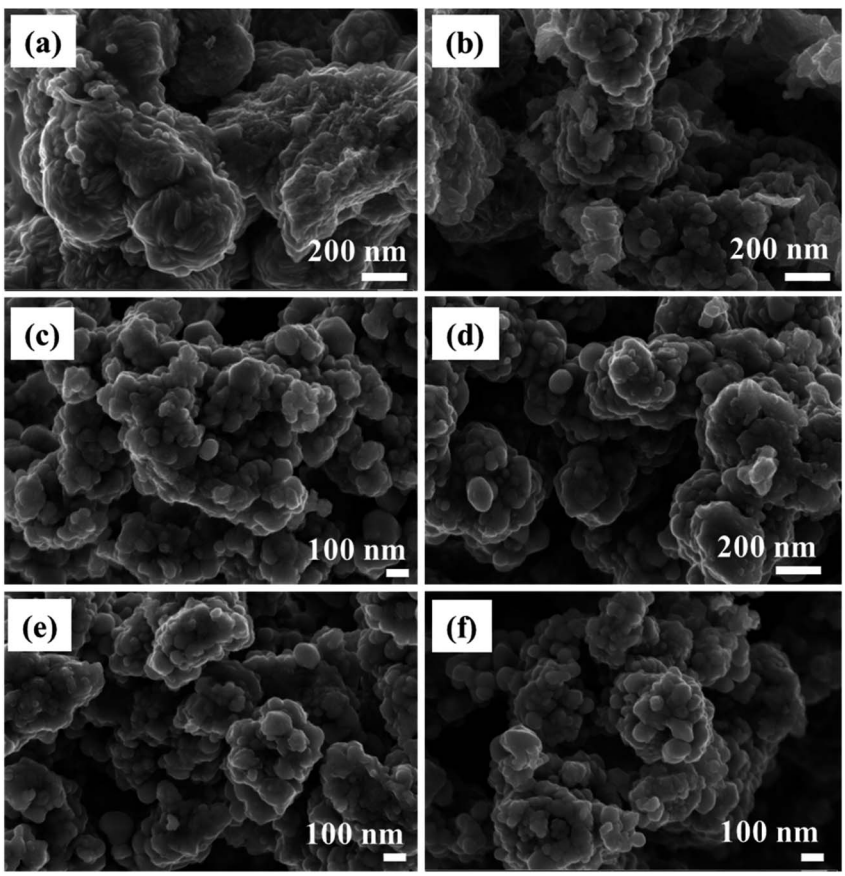

Fig. 2 SEM images of $Ni_{(1-x)}Cu_xCo_2S_4$ [where x is (a) 0, (b) 0.2, (c) 0.4, (d) 0.6, (e) 0.8 and (f) 1] nanoparticles.

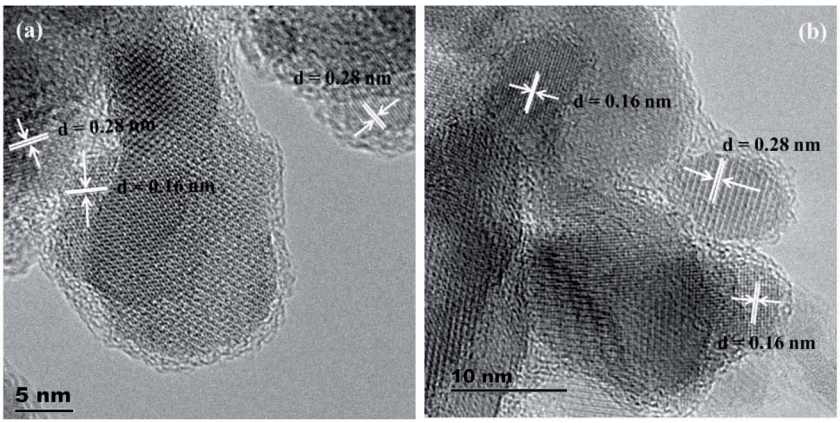

Fig. 3 Representative HRTEM images of $Ni_{(1-x)}Cu_xCo_2S_4$ solid solutions for (a) $x = 0.2$ (a) and (b) $x = 0.8$.

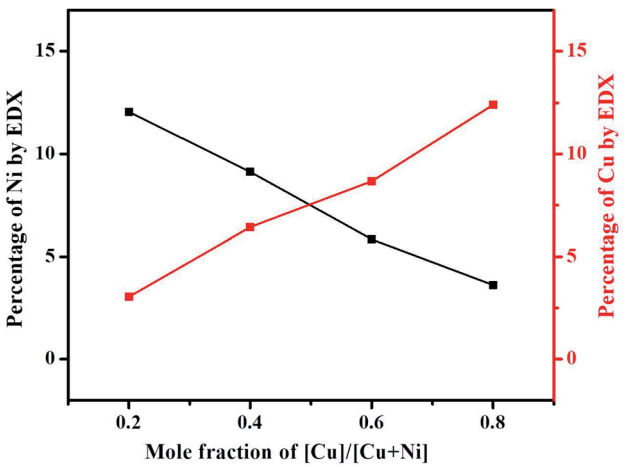

Fig. 4 A change of the content of copper and nickel as a function of mole fraction of [Cu]/[Cu + Ni] in precursor feed.

were found to be 9.39 Å, matching those reported in the standard data (9.387 Å, ICDD #: 00-020-0782). Upon incorporation of copper, a slight increase of the lattice parameters is seen (Table 1), which is also attributed to the larger size of Cu^{2+}. The dependence of the lattice parameters on the copper mole fraction used in the precursor feed shows a linear increase with a correlation coefficient of $r = 0.89$ (Fig. 1b). A similar dependence of the cell volume on the concentration of copper is seen (Table 1 and inset in Fig. 1b). This again suggests that the intended solid solutions were successfully prepared as the large incoming ion is expected to cause a slight expansion of the host cell.[7] The lattice constant and cell volume obtained for pure $CuCo_2S_4$ (9.45 Å and 843.9 $Å^3$, respectively) are also comparable with the values reported in the standard data (9.474 Å and 850.35 $Å^3$, ICDD #: 00-042-1450). The estimation of average particle sizes of the solid solutions was made based on the Scherrer equation. The sizes appear to be slightly larger than that of pure $NiCo_2S_4$ (Table 1). This is consistent with the relatively broad peaks observed in the absence of copper ions.

The morphology of $NiCo_2S_4$, $CuCo_2S_4$, and the solid solutions was examined by TEM and SEM. The SEM images reveal quasi-spherical nanoparticles forming agglomerates (Fig. 2 and S3†). TEM analysis similarly shows agglomerated particles but with less-defined morphology (Fig. S4†). It can be seen that incorporating Cu^{2+} into the crystal structure of $NiCo_2S_4$ has no significant effect on the morphology of the particles. The observed agglomeration can be a result of the absence of a capping agent in the synthesis. While the melt method can adopt a 'self-capping' approach, effective capping is commonly achieved with long alkyl chain precursors. For instance, O'Brien *et al.*[42] prepared a long alkyl chain dithiocarbamate complex of cadmium, $[Cd(S_2CNMe(C_{18}H_{37}))_2]$ and employed it in the solvent-less synthesis of CdS quantum dots. The resultant particles were shown to be capped by the amine group $(HNMe(C_{18}H_{37}))$ produced during the decomposition of the precursor. Self-capped Bi_2S_3 quantum dots were similarly synthesized *via* the solvent-less thermolysis of $[Bi(S_2CNMe^{n}octadecyl)_3]$.[43] Copper sulfide nanoparticles synthesized by Akhtar *et al.* *via* solvent-less thermolysis of bis(*O*-ethylxanthato)copper(II) showed a tendency of particle–particle agglomeration, whereas the nanoparticles synthesized from the longer alkyl chain complex, bis(*O*-octylxanthato)copper(II) exhibited well-defined morphologies due to better capping.[44] Thus, the aggregation observed for the synthesized $Ni_{(1-x)}Cu_xCo_2S_4$ $(0 \leq x \leq 1)$ nanoparticles can also be a result of the short alkyl chain xanthate complexes employed.

The HRTEM images of two representative samples of the solid solutions ($Ni_{(1-x)}Cu_xCo_2S_4$, $x = 0.2$ and 0.8) are presented in Fig. 3. The images show lattice fringes with a *d*-spacing of 0.28 nm, which corresponds to the (311) and (113) planes of $NiCo_2S_4$ and $CuCo_2S_4$, respectively, and lattice fringes with a *d*-spacing of 0.16 nm, which matches that of the (440) and (044) planes of $NiCo_2S_4$ and $CuCo_2S_4$ respectively.

EDX analysis was carried out to examine the elemental composition of the synthesized materials. The EDX spectrum of $NiCo_2S_4$ ($Ni_{(1-x)}Cu_xCo_2S_4$, $x = 0$) indicates the presence of only Ni, Co, and S (Fig. S5a†), whereas the EDX spectrum of $CuCo_2S_4$ ($Ni_{(1-x)}Cu_xCo_2S_4$, $x = 1$) indicates the presence of only Cu, Co, and S (Fig. S5f†). On the other hand, the EDX spectra of the solid solutions show the presence of Ni, Cu, Co, and S (Fig. S5(b–e)†). The percentage atomic composition and mole composition of

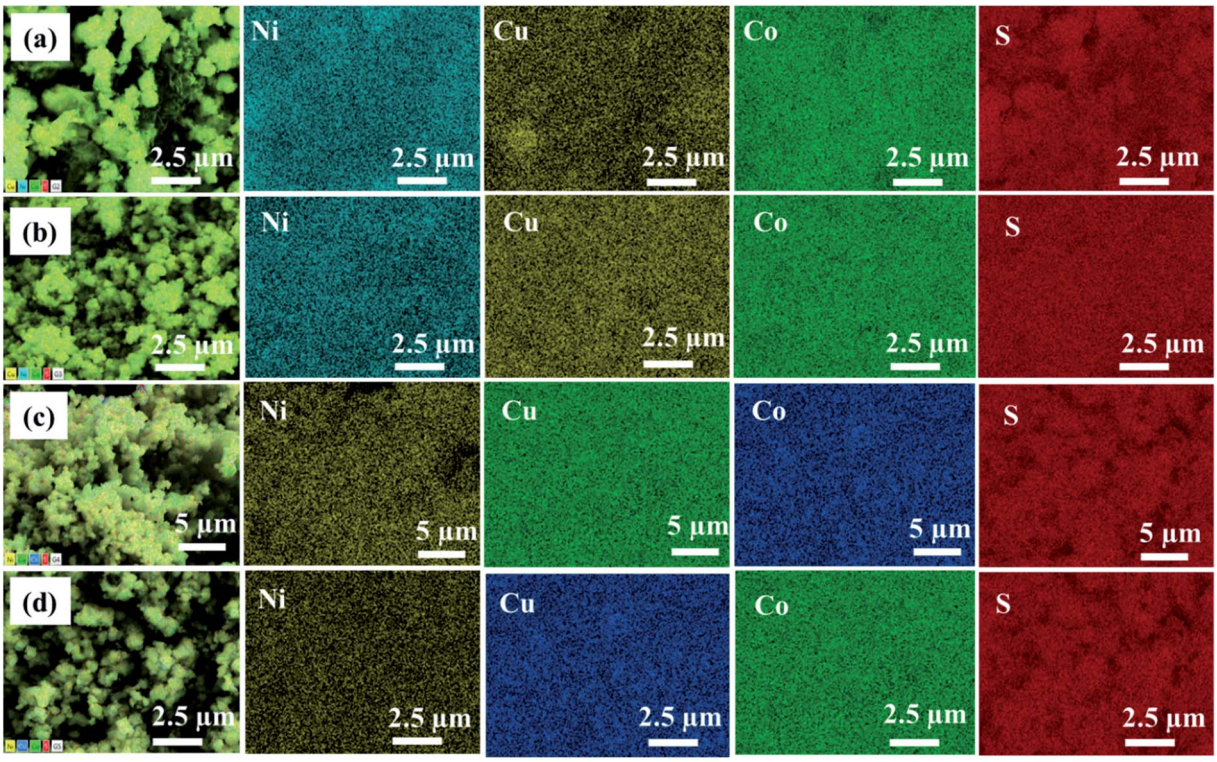

Fig. 5 EDX elemental mapping of $Ni_{(1-x)}Cu_xCo_2S_4$ (x = 0.2, 0.4, 0.6 and 0.8) nanoparticles showing a uniform distribution of elements.

the synthesized systems are presented in Tables S1† and 1, respectively. It can be seen that all experimental values compare well with the theoretical values with slight deviations. The observed deviations might be caused by inadequate mixing of the solid precursors and precursor reactive melts, as well as small losses which can occur during material transfer. As expected, a plot of the percentage of Ni and Cu observed from EDX as a function of mole fraction of [Cu]/[Cu + Ni] in precursor feed shows a continuous decrease in the content of nickel with a constant increase in copper content (Fig. 4). All these observations suggest the successful formation of $Ni_{(1-x)}Cu_xCo_2S_4$ ($0.2 \leq x \leq 0.8$) solid solutions. EDX mapping of all the solid solutions shows a uniform distribution of the respective elements in the systems (Fig. 5).

3.2 Electrochemical properties of $Ni_{(1-x)}Cu_xCo_2S_4$ ($0 \leq x \leq 1$)

Henceforth, $Ni_{(1-x)}Cu_xCo_2S_4$ synthesized at x = 0, 0.2, 0.4, 0.6, 0.8 and 1 will be referred to as NCS, NCCS-1, NCCS-2, NCCS-3, NCCS-4 and CCS respectively. For comparison, the electrochemical properties of the solid solutions, as well as those of pristine $NiCo_2S_4$ and $CuCo_2S_4$ have been studied.

3.2.1. Charge storage performance. The capacity of the electrodes containing synthesized nanomaterials $Ni_{(1-x)}Cu_xCo_2S_4$ ($0 \leq x \leq 1$) was determined from cyclic voltammograms (CV) and galvanostatic charge–discharge (GCD) curves. Fig. 6a shows the representative voltammogram of the NCCS-2 electrode at various scan rates (2–300 mV s^{-1}) within the potential range 0–0.6 V (V, *vs.* Hg/HgO). Broad redox peaks are seen with a clear maximum of the anodic peak seen only at a low scan rate, indicating pseudocapacitive behavior of NCCS-2.[45] Some differences in the shape of CV curves and clear appearance of both anodic and cathodic peaks depends on the sample composition (Fig. S6†). The latter effect may result from the electrooxidation of the mixed metal sulfide:[46,47]

$$NiCo_2S_4 + 2OH^- \leftrightarrow NiSOH + 2CoSOH + 2e^- \quad (1)$$

$$CuCo_2S_4 + 2OH^- \leftrightarrow CuSOH + 2CoSOH + 2e^- \quad (2)$$

$$CoSOH + OH^- \leftrightarrow CoSO + H_2O + e^- \quad (3)$$

With the increase of scan rate, the shift of anodic and cathodic peaks towards positive and negative potential, respectively, was noticed (Fig. 6a and S6†). This phenomenon is attributed to the polarization effect of the electrode at a higher scan rate.[48] The GCD curves recorded at the current density of 1 to 30 A g^{-1} show non-linearity (Fig. 6b and S7†). They are typical for pseudocapacitors and can be divided into three sections: (i) potential decay, (ii) plateau region, and (iii) potential drop. The potential decay results from internal resistance, and the second plateau region can be ascribed to the faradaic redox reactions (1)–(3). The last potential drop is due to the electric double-layer charging.[45] Importantly, the GCD curves of NCCS-2 show a longer discharge time, indicative of high charge storage capability. The dependence of specific capacitance on the current density was calculated by the following equation:[49]

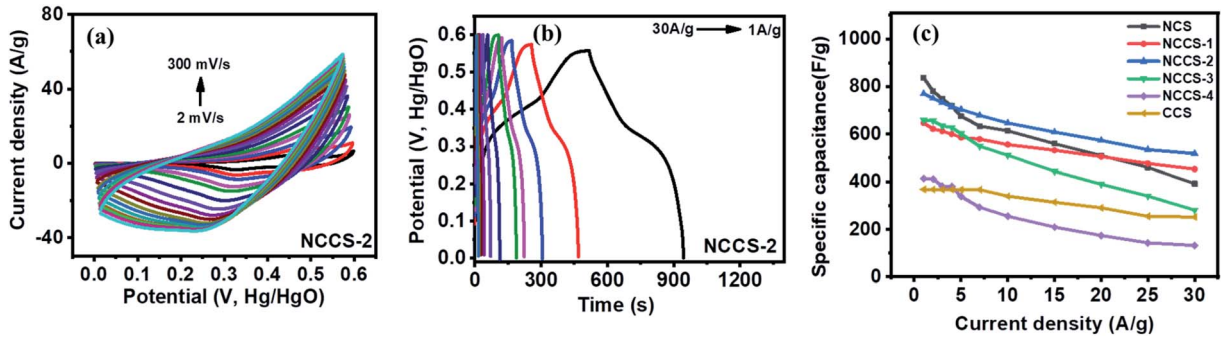

Fig. 6 (a) Cyclic voltammetry curve of the NCCS-2 electrode at various scan rates of 2–300 mV s^{-1}, (b) GCD curves of the NCCS-2 electrode at various current densities of 1–30 A g^{-1}, and (c) variation of specific capacitance *versus* current density for all electrodes.

$$C = \frac{I \times \Delta t}{\Delta V \times m} \quad \text{(i)}$$

where I is discharge current, Δt is discharge time, ΔV is operating potential range and m is the mass of the $Ni_{(1-x)}Cu_xCo_2S_4$ ($0 \leq x \leq 1$) electrodes. For all samples, this dependence on current density (Fig. 6c) is rather monotonic. However, the dependence of the specific capacitance on the sample composition is different for the lowest and highest current density. At lowest current density the specific capacitance increases in the order CCS (368 F g^{-1}) < NCCS-4 (413 F g^{-1}) < NCCS-1 (647 F g^{-1}) < NCCS-3 (658 F g^{-1}) < NCCS-2 (770 F g^{-1}) < NCS (838 F g^{-1}), indicating that the specific capacitance of $CuCo_2S_4$ (CCS) is enhanced by substitution of Cu by Ni. On the other hand, at the highest current density, the specific capacitance of NCCS-2 and NCCS-3 electrodes is higher than that of NCS, indicating the optimal composition of the solid solution electrode.

While the change in composition decreases the specific capacitance of NCS, the capacitance is higher than that of the other electrodes at the lowest current density of 1 A g^{-1}. When current density increases from 1 to 30 A g^{-1}, the capacitance retention of the electrodes is 47, 70, 67, 43, 32, and 68% for NCS,

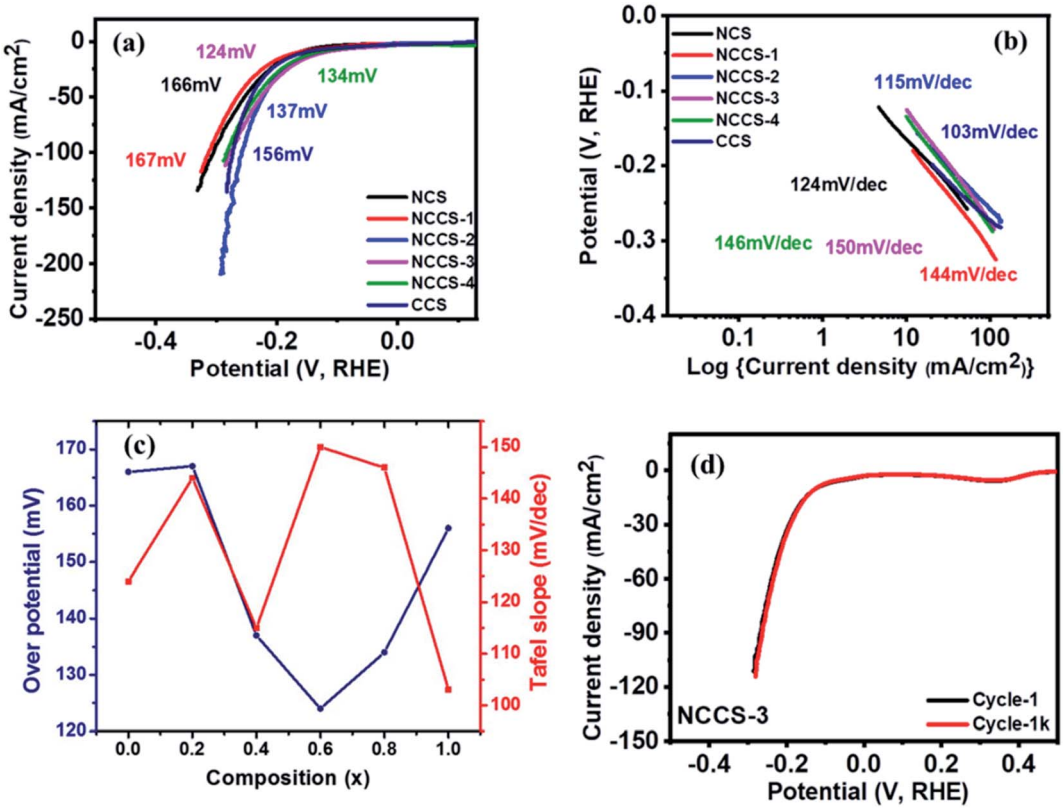

Fig. 7 (a) LSV curves for HER of all the $Ni_{(1-x)}Cu_xCo_2S_4$ ($0 \leq x \leq 1$) electrodes with corresponding overpotentials. (b) Tafel plots and Tafel slopes for all the $Ni_{(1-x)}Cu_xCo_2S_4$ ($0 \leq x \leq 1$) electrodes. (c) Variation of the overpotentials and Tafel slopes with composition for all the electrodes. (d) 1st and 1k cycle HER LSV curves for NCCS-3.

NCCS-1, NCCS-2, NCCS-3, NCCS-4, and CCS, respectively. The NCS electrode exhibits the highest specific capacitance of 838 F g^{-1} at 1 A g^{-1}, but for the same material, more than half the decrease in specific capacitance at the current density of 30 A g^{-1} is observed. On the other hand, the NCCS-2 electrode exhibits a lower specific capacitance of 770 F g^{-1} at 1 A g^{-1} as compared to NCS, but capacitance retention (67%) is higher (current density 1–30 A g^{-1}). These results show that the capacitance retention of $NiCo_2S_4$ is improved by the introduction of Cu in its structure.

Theoretically, the incorporation of Cu can change the charge state density and bandgap, as heteroatom metals tend to occupy positions in the crystal structure, thereby generating more active sites and improving conductivity.[26] However, since the theoretical capacitance of $CuCo_2S_4$ is lower than that of $NiCo_2S_4$,[31,50] incorporating excessive amounts of Cu can diminish the supercapacitive behavior of the material, as can be seen in Fig. 6c. A comparison of the NCS and NCCS-2 electrodes prepared in this study with other earlier reported nickel and cobalt sulfide-based electrode materials is presented in Table S2.† Although there are reported electrodes with better electrochemical performance, it can be seen that the specific capacitance displayed by NCS and NCCS-2 is comparable or better than the capacity of some previously reported nickel and cobalt sulfide-based electrodes.

3.2.2. Hydrogen evolution reaction (HER) and oxygen evolution reaction (OER). The electrocatalytic performance towards HER at $Ni_{(1-x)}Cu_xCo_2S_4$ ($0 \leq x \leq 1$) electrodes was investigated in aqueous 1 M KOH by linear sweep voltammetry. It was observed that the activity of the electrodes changes as the Cu content increases, thus it is important to find the optimal Cu content in the sample. As seen in Fig. 7(a), when $x = 0.2$, the change of overpotential is negligible. However, a further increase of Cu content resulted in a more significant change of the overpotential with a minimal value of 124 mV (for $x = 0.6$) to produce HER current density of 10 mA cm^{-2}. Fig. 7(b) shows the Tafel slope of all electrodes, which was computed by the following equation: $\eta = a + b \log j$; where η is potential, a is constant, b is the Tafel slope, and j is the current density.[36] The value of the Tafel slope also depends on Cu content in the sample. Interestingly the value of the Tafel slope is highest (150 mV dec^{-1}) for the NCCS-3 electrode exhibiting the lowest HER overpotential, and the lowest value (103 mV dec^{-1}) is seen for the electrode where all Ni is replaced by Cu. Such relation between Tafel slope and the overpotential has been recently reported.[51,52] Zhu *et al.* prepared Co-doped VSe_2 nanosheets with varying concentration of cobalt [$V_{1-x}Co_xSe_2$ (x = 0, 0.10, 0.14, 0.18, 0.22)] and investigated their HER performance.[51] They observed that to achieve a current density of 10 mA cm^{-2}, $V_{0.90}Co_{0.1}Se_2$ and $V_{0.82}Co_{0.18}Se_2$ required overpotential of 262 mV and 243 mV, with Tafel slopes of 65 and 83, respectively. Likewise, Zhang *et al.* investigated the HER performance of MoS_2 nanosheets doped with different concentrations of Mn and observed that the Tafel slope of one of the samples (0.5-Mn–MoS_2) was even lower than the Pt plate, despite having much higher overpotential as compared to Pt plate.[52] It is suggested that the change in Tafel slopes is due to a change in reaction kinetics of the samples. The variation of the HER overpotentials and Tafel slopes with composition for all the electrodes is shown in Fig. 7(c). A comparison between HER parameters of the solid solution $Ni_{(1-x)}Cu_xCo_2S_4$ ($x = 0.6$) electrode and other reported NiS and CoS-based electrodes having different

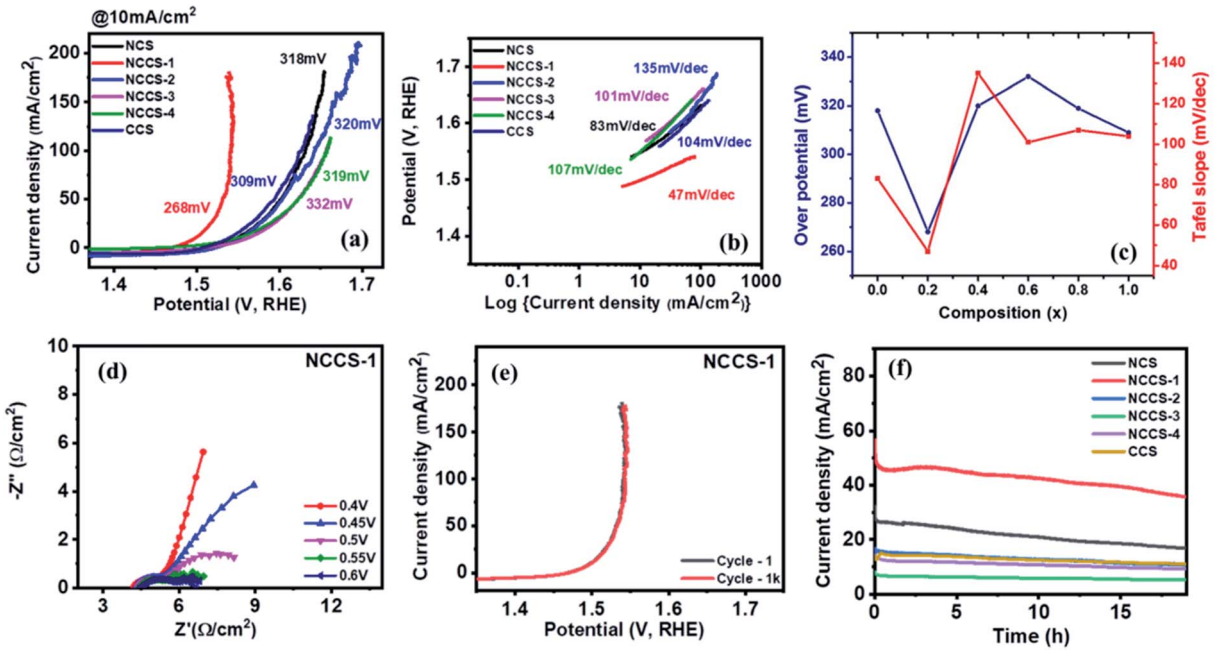

Fig. 8 (a) OER polarization curves for all the $Ni_{(1-x)}Cu_xCo_2S_4$ ($0 \leq x \leq 1$) electrodes. (b) Tafel slopes for all the $Ni_{(1-x)}Cu_xCo_2S_4$ ($0 \leq x \leq 1$) electrodes. (c) The variation of the OER overpotentials and Tafel slopes with composition for all electrodes. (d) Nyquist plot of NCCS-1 at various potential (*V vs.* SCE), (e) 1st and 1k cycle OER polarization curves for NCCS-1. (f) CA curves for all electrodes.

morphology and structure is shown in Table S3.† The comparison of the 1st and 1k LSV curves (Fig. 7(d) and S8†) indicates the durability of all prepared electrodes.

The OER performance of the $Ni_{(1-x)}Cu_xCo_2S_4$ ($0 \leq x \leq 1$) electrode was also investigated in 1 M KOH electrolyte. Clearly, both overpotential (at a current density of 10 mA cm^{-2}) (Fig. 8a) and Tafel plot depends on the solid solution composition (Fig. 8b). However, it is only for $x = 0.2$ (NCCS-1), where a significant decrease of overpotential to 268 mV, as compared with other electrodes (309–332 mV), is seen. Similarly, the NCCS-1 electrode exhibits significantly higher activity as determined by the lowest Tafel slope (47 mV dec^{-1}) than other electrodes. The variation of the OER overpotentials and Tafel slopes with composition for all electrodes is shown in Fig. 8c. A comparison of the OER performance observed for NCCS-1 with other nickel and cobalt sulfide-based materials is shown in Table S4.†

To further analyze the kinetics of OER, electrochemical impedance spectroscopy (EIS) was performed at various potentials. As seen in Fig. 8d and S9,† the size of the semicircle decreases with increasing potential, suggesting increasing the charge transfer capacity at the interface between the $Ni_{(1-x)}Cu_xCo_2S_4$ ($0 \leq x \leq 1$) electrode and 1 M KOH. Clearly, the NCC-1 electrode exhibits the lowest charge transfer resistance (R_{ct}) of 2.5 Ω cm^{-2}. This result is compatible with that obtained by polarization curves.

The catalytic stability of the $Ni_{(1-x)}Cu_xCo_2S_4$ ($0 \leq x \leq 1$) electrode was tested using LSV and chronoamperometry (CA) measurements. The 1st and 1000th OER polarization curves are almost matching (Fig. 8e and S10†). More importantly, the most active NCCS-1 electrode exhibits the smallest (*ca.* 10%) current decay during first under potentiostatic conditions. Moreover, in Fig. 8f, current variation with time was measured for all electrodes using chronoamperometric (CA) measurements. After 18 hours, all electrodes showed only slight current density decay with no major change even after a long time. These two measurements for characterizing electrocatalytic stability have proven that the $Ni_{(1-x)}Cu_xCo_2S_4$ ($0 \leq x \leq 1$) electrode has superior stability, which is crucial for real application.

These results indicate the importance of stoichiometry on electrocatalytic performance. In water-splitting, HER is a relatively straightforward cathodic half-reaction whereas OER is more complex of the two half-reactions and usually responsible for the low efficiency of the electrolyzer devices. Therefore, they are affected differently by a change in composition. Since the addition of copper can induce changes in the density of states and can generate different active sites by occupying a position in the crystal structure, the optimum concentration for enhancing the performance of electrodes is different for both HER and OER. In the present study it was shown that, for HER, the lower concentration of copper was not sufficient to promote the electrochemical performance of ternary $NiCo_2S_4$, and the optimum performance was observed for NCCS-3, whereas, for OER, only a lower concentration of copper was best for optimized performance. The higher amount may induce structural changes/defects in the crystal lattice that might be responsible for a decrease in OER performance.

4 Conclusion

To conclude, solid solutions of $Ni_{(1-x)}Cu_xCo_2S_4$ ($0.2 \leq x \leq 0.8$) have been successfully synthesized *via* solvent-less pyrolysis of respective metal ethyl xanthate complexes at 250 °C. p-XRD analysis confirms the formation of a uniform $Ni_{(1-x)}Cu_xCo_2S_4$ ($0.2 \leq x \leq 0.8$) solid solution over an entire range. Electrochemical characterization indicates that both the supercapacitive and electrocatalytic properties of the synthesized solid solutions vary with composition (Ni/Cu molar content). The specific capacitances of the solid solutions were in the order NCCS-2 (770 F g^{-1}) > NCCS-3 (658 F g^{-1}) > NCCS-1 (647 F g^{-1}) > NCCS-4 (413 F g^{-1}). The best HER and OER performance was observed for NCCS-3 and NCCS-1, which required the lowest overpotentials of 124 mV and 268 mV respectively, to deliver a current density of 10 mA cm^{-2}. The prepared electrodes further demonstrated high stability as well as durability. The formation of the solid solutions of $NiCo_2S_4$ and $CuCo_2S_4$ generally improves the electrochemical activity of the materials in the optimal ratio of Cu/Ni. These results might be of great importance as an alternative to complex solid solutions of transition metals.[53]

Based on theory and experimental experience, Cu increases conductivity and stability, which improve energy storage and conversion performance.[54,55] We introduced Cu^{2+} in the $NiCo_2S_4$ material, and the electrochemical properties such as energy storage and conversion showed great improvements in its properties in the optimal ratio of Cu. Apart from the synergistic effect of the metal cations, the synthetic method used in this study is also of interest as it yields uncapped nanomaterials, which is also beneficial for electrochemical performance. It has been reported that, in some cases, the presence of passivating ligands on the surface of nanomaterials can act as impurities, blocking the materials' active sites and diminishing the electrochemical performance.[56–58] It has further been shown that the use of long alkyl chain precursors in the melt synthesis of nanomaterials, which leaves a significant amount of carbonaceous materials on the surface, can similarly deteriorate the electrochemical performance.[35] Therefore melt method and the short alkyl chain precursors employed herein thus guarantee the synthesis of solid solutions free of surface carbonaceous/insulating materials for enhanced electrochemical performance.

Conflicts of interest

The authors declare no conflict of interest.

Acknowledgements

The authors are grateful to the National Research Foundation (NRF) South African Research Chairs Initiative (SARChI) for financial support. M. D. K. thanks the European Union's Horizon 2020 Research and Innovation Programme under the Marie Sklodowska-Curie grant agreement no. 847413 for funding. Scientific work published as part of an international co-financed project funded from the programme of the Minister

of Science and Higher Education entitled "PMW" in the years 2020–2024; agreement no. 5005/H2020-MSCA-COFUND/2019/2.

References

1 B. Liu, *et al.*, Semiconductor solid-solution nanostructures: synthesis, property tailoring, and applications, *Small*, 2017, **13**, 1701998.
2 M. Singh, S. o. Lara and S. Tlali, Effects of size and shape on the specific heat, melting entropy and enthalpy of nanomaterials, *J. Taibah Univ. Sci.*, 2017, **11**, 922–929.
3 S. A. Saah, *et al.*, Facile synthesis of a $PbS_{1-x}Se_x$ ($0 \leq x \leq 1$) solid solution using bis (N, N-diethyl-N′-naphthoylchalcogenoureato) lead (ii) complexes, *New J. Chem.*, 2018, **42**, 16602–16607.
4 T. Alqahtani, *et al.*, Synthesis of Bi 2− 2x Sb 2x S 3 ($0 \leq x \leq 1$) solid solutions from solventless thermolysis of metal xanthate precursors, *J. Mater. Chem. C*, 2018, **6**, 12652–12659.
5 M. Lusi, A rough guide to molecular solid solutions: design, synthesis and characterization of mixed crystals, *CrystEngComm*, 2018, **20**, 7042–7052.
6 U. Mizutani, Hume-Rothery rules for structurally complex alloy phases, *MRS Bull.*, 2012, **37**, 169.
7 L. Vegard and H. Schjelderup, Constitution of mixed crystals, *Phys. Z.*, 1917, **18**, 93–96.
8 M. D. Khan, *et al.*, Controlled synthesis of Sb2 (S1–x Se x) 3 ($0 \leq x \leq 1$) solid solution and the effect of composition variation on electrocatalytic energy conversion and storage, *ACS Appl. Energy Mater.*, 2020, **3**, 1448–1460.
9 J. Liu, H. Liu, F. Wang and Y. Song, Composition-controlled synthesis of Li x Co 3− x O 4 solid solution nanocrystals on carbon and their impact on electrocatalytic activity toward oxygen reduction reaction, *RSC Adv.*, 2015, **5**, 90785–90796.
10 P. Kulkarni, S. Nataraj, R. G. Balakrishna, D. Nagaraju and M. Reddy, Nanostructured binary and ternary metal sulfides: synthesis methods and their application in energy conversion and storage devices, *J. Mater. Chem. A*, 2017, **5**, 22040–22094.
11 C. Gervas, *et al.*, Synthesis of Off-Stoichiometric CoS Nanoplates from a Molecular Precursor for Efficient H2/O2 Evolution and Supercapacitance, *ChemElectroChem*, 2019, **6**, 2560–2569.
12 L.-L. Feng, *et al.*, High-index faceted Ni3S2 nanosheet arrays as highly active and ultrastable electrocatalysts for water splitting, *J. Am. Chem. Soc.*, 2015, **137**, 14023–14026.
13 X. Y. Yu and X. W. Lou, Mixed metal sulfides for electrochemical energy storage and conversion, *Adv. Energy Mater.*, 2018, **8**, 1701592.
14 D. J. Vaughan, R. G. Burns and V. M. Burns, Geochemistry and bonding of thiospinel minerals, *Geochim. Cosmochim. Acta*, 1971, **35**, 365–381.
15 Y. Zhang, *et al.*, Shape-controlled synthesis of NiCo 2 S 4 and their charge storage characteristics in supercapacitors, *Nanoscale*, 2014, **6**, 9824–9830.
16 F. Zhu, H. Xia and T. Feng, Nanowire interwoven NiCo2S4 nanowall arrays as promising anodes for lithium ion batteries, *Mater. Technol.*, 2015, **30**, A53–A57.
17 A. Banerjee, *et al.*, Nickel cobalt sulfide nanoneedle array as an effective alternative to Pt as a counter electrode in dye sensitized solar cells, *RSC Adv.*, 2014, **4**, 8289–8294.
18 J. Jiang, *et al.*, A PEGylated deep eutectic solvent for controllable solvothermal synthesis of porous NiCo 2 S 4 for efficient oxygen evolution reaction, *Green Chem.*, 2017, **19**, 3023–3031.
19 L. Ma, *et al.*, Self-assembled ultrathin NiCo2S4 nanoflakes grown on Ni foam as high-performance flexible electrodes for hydrogen evolution reaction in alkaline solution, *Nano Energy*, 2016, **24**, 139–147.
20 C. Xia, P. Li, A. N. Gandi, U. Schwingenschlögl and H. N. Alshareef, Is NiCo2S4 really a semiconductor?, *Chem. Mater.*, 2015, **27**, 6482–6485.
21 L. Nie, H. Wang, Y. Chai, S. Liu and R. Yuan, In situ formation of flower-like CuCo 2 S 4 nanosheets/graphene composites with enhanced lithium storage properties, *RSC Adv.*, 2016, **6**, 38321–38327.
22 Y. Gong, J. Zhao, H. Wang and J. Xu, CuCo2S4/reduced graphene oxide nanocomposites synthesized by one-step solvothermal method as anode materials for sodium ion batteries, *Electrochim. Acta*, 2018, **292**, 895–902.
23 L.-Q. Fan, *et al.*, Synthesis of CuCo2S4 nanosheet arrays on Ni foam as binder-free electrode for asymmetric supercapacitor, *Int. J. Hydrogen Energy*, 2018, **43**, 23372–23381.
24 C. Zequine, *et al.*, Effect of solvent for tailoring the nanomorphology of multinary CuCo2S4 for overall water splitting and energy storage, *J. Alloys Compd.*, 2019, **784**, 1–7.
25 S. Czioska, J. Wang, X. Teng and Z. Chen, Hierarchically structured CuCo2S4 nanowire arrays as efficient bifunctional electrocatalyst for overall water splitting, *ACS Sustainable Chem. Eng.*, 2018, **6**, 11877–11883.
26 M. Zhang, *et al.*, Boosting Energy and Power of Cu-doped NiCo2S4/graphite Electrode for High Performance Supercapacitors, *J. Alloys Compd.*, 2022, 163633.
27 D. Li, Y. Gong and C. Pan, Facile synthesis of hybrid CNTs/NiCo 2 S 4 composite for high performance supercapacitors, *Sci. Rep.*, 2016, **6**, 29788.
28 M. Yan, *et al.*, Construction of a hierarchical NiCo2S4@ PPy core–shell heterostructure nanotube array on Ni foam for a high-performance asymmetric supercapacitor, *ACS Appl. Mater. Interfaces*, 2016, **8**, 24525–24535.
29 S. Raj, S. K. Srivastava, P. Kar and P. Roy, Three-dimensional NiCo 2 O 4/NiCo 2 S 4 hybrid nanostructure on Ni-foam as a high-performance supercapacitor electrode, *RSC Adv.*, 2016, **6**, 95760–95767.
30 J. Zhu, *et al.*, Wearable High-Performance Supercapacitors Based on Silver-Sputtered Textiles with FeCo2S4–NiCo2S4 Composite Nanotube-Built Multitripod Architectures as Advanced Flexible Electrodes, *Adv. Energy Mater.*, 2017, **7**, 1601234.
31 W. Chen, *et al.*, Formation of mixed metal sulfides of NixCu1− xCo2S4 for high-performance supercapacitors, *J. Electroanal. Chem.*, 2019, **836**, 134–142.
32 J. A. Wasastjerna, *On the radii of ions*, Soc. Scientiarum Fennica, 1923.

33 T. Wagner and N. J. Cook, Carrollite and related minerals of the linnaeite group; solid solutions and nomenclature in the light of new data from the Siegerland District, Germany, *Can. Mineral.*, 1999, **37**, 545–558.

34 E. Lewis, S. Haigh and P. O'Brien, The synthesis of metallic and semiconducting nanoparticles from reactive melts of precursors, *J. Mater. Chem. A*, 2014, **2**, 570–580.

35 G. B. Shombe, *et al.*, Direct solvent free synthesis of bare α-NiS, β-NiS and α-β-NiS composite as excellent electrocatalysts: effect of self-capping on supercapacitance and overall water splitting activity, *Sci. Rep.*, 2020, **10**, 1–14.

36 G. B. Shombe, *et al.*, Unusual doping induced phase transitions in NiS via solventless synthesis enabling superior bifunctional electrocatalytic activity, *Sustainable Energy Fuels*, 2020, **4**, 5132–5143.

37 D. Ung and B. M. Cossairt, Effect of surface ligands on CoP for the hydrogen evolution reaction, *ACS Appl. Energy Mater.*, 2019, **2**, 1642–1645.

38 M. D. Khan, M. Aamir, G. Murtaza, M. A. Malik and N. Revaprasadu, Structural investigations of SnS 1− x Se x solid solution synthesized from chalcogeno-carboxylate complexes of organo-tin by colloidal and solvent-less routes, *Dalton Trans.*, 2018, **47**, 10025–10034.

39 M. D. Khan, G. Murtaza, N. Revaprasadu and P. O'Brien, Synthesis of chalcopyrite-type and thiospinel minerals/materials by low temperature melts of xanthates, *Dalton Trans.*, 2018, **47**, 8870–8873.

40 C. Zequine, *et al.*, High-performance flexible supercapacitors obtained via recycled jute: bio-waste to energy storage approach, *Sci. Rep.*, 2017, **7**, 1–12.

41 M. D. Khan, *et al.*, Electrochemical investigation of uncapped AgBiS 2 (schapbachite) synthesized using in situ melts of xanthate precursors, *Dalton Trans.*, 2019, **48**, 3714–3722.

42 M. Lazell and P. O'Brien, A novel single source precursor route to self capping CdS quantum dots, *Chem. Commun.*, 1999, 2041–2042.

43 M. Lazell, S. J. Nørager, P. O'Brien and N. Revaprasadu, The use of dithio-and diselenocarbamates as precursors to nanoscale materials, *Mater. Sci. Eng., C*, 2001, **16**, 129–133.

44 M. Akhtar, *et al.*, Phase controlled synthesis of copper sulfide nanoparticles by colloidal and non-colloidal methods, *Mater. Chem. Phys.*, 2016, **180**, 404–412.

45 D. Guragain, *et al.*, Effect of dopant on the morphology and electrochemical performance of Ni 1-x Ca x Co 2 O 4 (0= x= 0.8) oxide hierarchical structures, *MRS Adv.*, 2020, **5**, 2487–2494.

46 K. Yang, L.-Z. Fan, J. Guo and X. Qu, Significant improvement of electrochemical properties of AlF3-coated LiNi0. 5Co0. 2Mn0. 3O2 cathode materials, *Electrochim. Acta*, 2012, **63**, 363–368.

47 H. You, *et al.*, Bubble-supported engineering of hierarchical CuCo 2 S 4 hollow spheres for enhanced electrochemical performance, *J. Mater. Chem. A*, 2018, **6**, 5265–5270.

48 R. Nie, *et al.*, Pulsed laser deposition of NiSe2 film on carbon nanotubes for high-performance supercapacitor, *Eng. Sci.*, 2018, **6**, 22–29.

49 G. He, *et al.*, S, N-Co-doped graphene-nickel cobalt sulfide aerogel: improved energy storage and electrocatalytic performance, *Adv. Sci.*, 2017, **4**, 1600214.

50 T. Chen, S. Wei and Z. Wang, NiCo2S4-based composite materials for supercapacitors, *ChemPlusChem*, 2020, **85**, 43–56.

51 Q. Zhu, *et al.*, One-pot synthesis of Co-doped VSe2 nanosheets for enhanced hydrogen evolution reaction, *ACS Appl. Energy Mater.*, 2018, **2**, 644–653.

52 L. Zhang, *et al.*, Synergistically configuring intrinsic activity and fin-tube-like architecture of Mn-doped MoS2-based catalyst for improved hydrogen evolution reaction, *ACS Appl. Energy Mater.*, 2018, **2**, 493–502.

53 T. Löffler, *et al.*, Toward a paradigm shift in electrocatalysis using complex solid solution nanoparticles, *ACS Energy Lett.*, 2019, **4**, 1206–1214.

54 W. C. Lee, L.-L. Tan, S. Sumathi and S.-P. Chai, Copper-doped flower-like molybdenum disulfide/bismuth sulfide photocatalysts for enhanced solar water splitting, *Int. J. Hydrogen Energy*, 2018, **43**, 748–756.

55 K. Pandey, P. Yadav and I. Mukhopadhyay, Elucidating the effect of copper as a redox additive and dopant on the performance of a PANI based supercapacitor, *Phys. Chem. Chem. Phys.*, 2015, **17**, 878–887.

56 D. Ung and B. M. Cossairt, The Effect of Surface Ligands on CoP for the Hydrogen Evolution Reaction, *ACS Appl. Energy Mater.*, 2019, **2**(3), 1642–1645.

57 Y. Lu, Y. Wang and W. Chen, Silver nanorods for oxygen reduction: strong effects of protecting ligand on the electrocatalytic activity, *J. Power Sources*, 2011, **196**, 3033–3038.

58 D. A. Henckel, O. Lenz and B. M. Cossairt, Effect of ligand coverage on hydrogen evolution catalyzed by colloidal WSe2, *ACS Catal.*, 2017, **7**, 2815–2820.